J. Plasma Physics (2015), *vol.* 81, 365810102
doi:10.1017/S002237781400066X

Characterization of laser-driven proton beams from near-critical density targets using copper activation

L. Willingale[1,†‡], S. R. Nagel[2,†], A. G. R. Thomas[1,†], C. Bellei[2,†], R. J. Clarke[3], A. E. Dangor[4], R. Heathcote[3], M. C. Kaluza[5,6], C. Kamperidis[4], S. Kneip[4], K. Krushelnick[1], N. Lopes[4,7], S. P. D. Mangles[4], W. Nazarov[8], P. M. Nilson[9,†] and Z. Najmudin[4]

[1]Center for Ultrafast Optical Science, University of Michigan, 2200 Bonisteel Boulevard, Ann Arbor, MI 48109, USA
[2]Lawrence Livermore National Laboratory, Livermore, CA 94551, USA
[3]Central Laser Facility, Rutherford Appleton Laboratory, Chilton, Oxon OX11 0QX, UK
[4]Blackett Laboratory, The John Adams Institute for Accelerator Science, Imperial College London SW7 2AZ, UK
[5]Institut für Optik und Quantenelektronik, Max-Wien-Platz 1, 07743 Jena, Germany
[6]Helmholtz Institute Jena, Frbelstieg 3, 07743 Jena, Germany
[7]GoLP, Instituto Superior Tecnico, Lisbon, Portugal
[8]High Energy Laser Materials R&D Laboratory, University of St Andrews, Unit 4, St Andrews NTC, North Haugh, St Andrews, Fife KY16 9ST, UK
[9]Laboratory for Laser Energetics, University of Rochester, Rochester, NY 14623, USA

(Received 28 May 2014; revised 10 July 2014; accepted 25 July 2014;
first published online 5 September 2014)

Copper activation was used to characterize high-energy proton beam acceleration from near-critical density plasma targets. An enhancement was observed when decreasing the target density, which is indicative for an increased laser-accelerated hot electron density at the rear target-vacuum boundary. This is due to channel formation and collimation of the hot electrons inside the target. Particle-in-cell simulations support the experimental observations and show the correlation between channel depth and longitudinal electric field strength is directly correlated with the proton acceleration.

1. Introduction

During the interaction of laser pulses with intensities exceeding $I > 1.4\times 10^{18}$ [W cm^{-2}]/λ_μ^2 [μm^2] (where λ_μ is the laser wavelength in microns) with a plasma, electrons oscillate at speeds approaching the speed of light, so relativistic effects are important. The exchange of energy between the laser pulse and the electrons is expected to be most efficient at the critical density surface (Pukhov and Meyer ter Vehn 1998). This leads to strong and rapid electron heating. Consequently shocks with a high Mach number can be launched into the plasma. From this shock wave ions can be reflected and accelerated to high energies (Silva et al. 2004). Recently it has been shown that this mechanism can generate quasi-monoenergetic proton beams using moderate-intensity CO_2 lasers ($\lambda = 10$ μm) (Haberberger et al. 2012). Numerical

† Previous address: Blackett Laboratory, Imperial College London SW7 2AZ, United Kingdom
‡ Email address for correspondence: wlouise@umich.edu

modeling shows favorable scaling of proton energy with laser intensity (Fiuza et al. 2012, 2013). Note that in the case of very high laser intensity, the reflecting shock can also be driven by the ponderomotive force of the laser (Palmer et al. 2011). The critical density is defined at low intensities as the density where the laser frequency ω_L equals the plasma frequency such that $n_c = m_e \epsilon_0 \omega_L^2 / e^2$, where m_e is the mass of an electron, ϵ_0 is the permittivity of free space, and e is the charge of an electron. The relativistic increase of the effective mass of the electron to $\langle \gamma \rangle m_e$, where $\langle \gamma \rangle$ is the time-averaged relativistic Lorentz factor, leads to an effective increase in the critical density for high-intensity laser pulses. This enables light to propagate up to the relativistic critical density $n_{\gamma c} = \langle \gamma \rangle n_c$, an effect known as relativistically induced transparency (RIT).

Due to the variety of different ion acceleration mechanisms, it is important to study the laser-plasma interaction at near-critical densities in more detail, especially with optical lasers that can achieve much higher intensities. However, it is not trivial to generate a near-critical density plasma with well-controlled conditions for optical wavelengths experimentally. High-power laser systems typically have central wavelengths of 800 nm or 1.054 μm and can be focused to intensities exceeding 10^{21} W cm^{-2}. For these wavelengths, $n_c = 1.75 \times 10^{21}$ cm^{-3} and $n_c = 1.01 \times 10^{21}$ cm^{-3} respectively and therefore a fully ionized solid foil target typically reaches densities $> 100 n_c$, very overdense, while gas targets typically can achieve underdense conditions of up to $\sim 0.1 n_c$. Pre-heated solid foils can be used to produce near-critical density targets, but it is difficult to precisely control the density conditions and there will be long-density scale-lengths on the laser-irradiated side. For a definitive study it would therefore be beneficial to have targets available showing uniform and near-critical density with steep gradients at the boundaries. Alternative targets are very low density foams that when fully ionized, produce a uniform, near-critical density plasma with sharp-density gradients. A different ion acceleration mechanism that uses RIT is the breakout-after-burner (BOA) mechanism (Albright et al. 2007). For this scheme, very thin solid density foils expand on a timescale shorter than the laser pulse duration to densities that are below $n_{\gamma c}$ so that energy exchange between the laser pulse to the ions via the electrons is efficient.

Experiments using these very low density foam targets have provided insight into the RIT channel formation process (Willingale et al. 2009, 2011). For densities $n_e < n_{\gamma c}$ the plasma is effectively underdense so that the ponderomotive force of the laser expels electrons from the regions of highest intensity to form a channel (Willingale et al. 2011). Here, it was found that the channel formation rate is much higher for $n_e < n_{\gamma c}$ than would be expected from the hole-boring model (Wilks et al. 1992). A simple model where the laser energy is equated with the energy transferred to the electrons to form the channel was shown to give good agreement with the numerical modeling channel depths such that $d \approx 0.25 c \tau_L (a_0/2)(n_c/n_e)$, where τ_L is the laser pulse duration and $a_0 = \sqrt{I \lambda_\mu^2 / (1.4 \times 10^{18} [\mathrm{W\,cm^{-2}}])}$ is the peak normalized vector potential of the laser pulse I which is the laser intensity in units of W cm^{-2}, and λ_μ is the laser wavelength in microns (Willingale et al. 2009, 2011). Associated with the channel are strong radial electric fields and self-generated azimuthal magnetic fields. These act to assist the collimation of the hot electrons and prevent the natural divergence of the accelerated beam. The deeper the channel penetrates the target ($d \propto n_e^{-1}$), the smaller the area that the hot electron beam emerges from at the rear side of the target. The hot electron density is related to the space charge field created at the vacuum interface and hence the maximum proton energies that are accelerated

from the rear target surface via sheath acceleration (Hatchett et al. 2000; Mora 2003). Therefore, measuring the spectra of the proton beams provides information about the channel length and the RIT (Willingale et al. 2009) or the energy transfer from the laser into the hot electrons (Albright et al. 2007; Henig et al. 2009).

The next generation of laser systems currently under construction is expected to attain intensities exceeding 10^{23} W cm^{-2}. In these extreme fields, solid density aluminum would become near-critical density due to RIT, and quantum-electrodynamic (QED) effects such as radiation damping, prolific pair production, and intense γ rays have been predicted (Ridgers et al. 2012, 2013). This makes understanding the RIT process at the current, more modest, intensities important before the additional complexities of QED will become relevant.

In this paper, details of the experiment by Willingale et al. (2009) characterizing RIT via proton acceleration are presented and discussed. In particular, the copper activation stack diagnostic is described in detail and additional observations from the particle-in-cell (PIC) simulations are given. Although the copper activation stack has been used in previous studies to diagnose the proton beam spectra (Clark 2001; Zepf et al. 2001; Wei et al. 2006), the possible contributions from additional reactions are discussed. Both the maximum proton energies and energy conversion efficiencies were enhanced when the target density was reduced towards the critical density. The interpretation of this trend was that the increased channel formation due to the RIT both assists electron acceleration and keeps the hot electrons collimated within the channel so that when the hot electrons emerge into the vacuum at the rear of the target, the electric field accelerating the protons was enhanced. Two-dimensional (2D) PIC simulations were performed to better understand the experimental results and show how the longitudinal electric field at the rear surface is affected for the different target densities.

2. Experimental set-up and copper activation stack proton beam diagnostic

The experiment was performed on the Vulcan Petawatt laser facility at the Rutherford Appleton Laboratory. The laser pulse had an energy of 270$\pm$70 J on target in a full-width-half-maximum (FWHM) pulse duration of 560$\pm$150 fs. An $f/3$ off-axis parabolic mirror focused the light to a 5.0 ± 0.5 μm diameter FWHM focal spot to produce a theoretical maximum cycle-averaged intensity of $(8.0 \pm 3.4) \times 10^{20}$ W cm^{-2} in vacuum. This corresponds to a normalized vector potential of $a_0 \approx 36$. The laser was linearly polarized with a central wavelength of 1.054 μm. Therefore the critical density is $n_c = 1.0 \times 10^{21}$ cm^{-3}.

The very low density foam targets fabricated using the *in situ* polymerization technique (similar to the technique described by Falconer et al. (1995) were mounted in 250-μm-thick aluminum washers to support the delicate structure. The foam composition was 71% C, 27% O, and 2% H by mass and had mass densities of $\rho =$ 3, 10, 15, 20, 45, and 100 mg cm^{-3}. When fully ionized, these would produce plasma densities of $n_e = 0.9n_c$, $3n_c$, $4.5n_c$, $6n_c$, $13.5n_c$, and $30n_c$. The foam targets were shot at 0° angle of incidence. For comparison, 10-μm thick Mylar targets were also shot, but at a 45° angle of incidence.

The spatially integrated proton spectra were measured using activation of copper. A stack of copper foils intercepts the proton beam, covering a half-angle of $\approx$25° and the consequent nuclear reactions produce positron emission isotopes that can be counted. This technique was first described for laser-accelerated proton beams by Clark (2001). For experiments where protons could be accelerated to energies

Reaction	Product	Peak X-section (barns)	Peak p or γ energy (MeV)	Threshold energy (MeV)	$T_{\frac{1}{2}}$ of product
^{63}Cu(p,n)	**^{63}Zn**	**≈ 0.5**	**≈ 11**	**4**	**38.47 m**
^{63}Cu(p,2n)	^{62}Zn	≈ 0.1	≈ 25	13	9.186 h
^{63}Cu(p,n+p)	**^{62}Cu**	**≈ 0.9**	**≈ 25**	**14**	**9.67 m**
^{63}Cu(γ,n)	**^{62}Cu**	**≈ 0.1**	**≈ 17**	**10**	**9.67 m**
^{63}Cu(p,2n+p)	^{61}Cu	≈ 0.3	≈ 35	20	3.333 h
^{63}Cu(p,n+p+α)	^{58}Co	≈ 0.2	≈ 40	26	70.86 d
^{65}Cu(p,n)	^{65}Zn	≈ 0.9	≈ 10	2	243.7 d
^{65}Cu(p,3n)	**^{63}Zn**	**≈ 0.16**	**≈ 35**	**30**	**38.47 m**
^{65}Cu(p,n+p)	^{64}Cu	≈ 0.6	≈ 24	13	12.70 h
^{65}Cu(γ,n)	^{64}Cu	≈ 0.15	≈ 18	10	12.70 h
^{65}Cu(p,X)	**^{62}Cu**	**≈ 0.2**	**≈ 50**	**30**	**9.67 m**

TABLE 1. The possible products from reactions with cross-sections $\geqslant 0.1$ barns which decay by β^+ emission from proton and γ interactions with ^{63}Cu and ^{65}Cu. The reactions producing ^{63}Zn and ^{62}Cu are highlighted.

>30 MeV, additional reactions are possible and need to be considered and accounted for. Copper occurs naturally as two isotopes, 69.2% is ^{63}Cu and the other 30.8% is ^{65}Cu. In addition to the tens of MeV energy protons, a high-intensity laser plasma interaction can produce large radiation fluxes of γ-rays and high-energy electrons (up to ~100 MeV) that can generate secondary γ-rays via bremsstrahlung as they propagate through the activation stack. Table 1 shows the possible products from nuclear reactions from incident protons and γ-rays and the cross-sections for the most prominent reactions are shown in Fig. 1. They are from the National Nuclear Data Center database. Other reactions that will occur are assumed to be negligible to the measurements due to a long half life, a small cross-section at the proton and γ energies expected, or because they create a stable product that would not be detected with this technique.

The nuclear reactions with the largest proton reaction cross-sections in ^{63}Cu are ^{63}Cu(p, n)^{63}Zn and ^{63}Cu(p, np)^{62}Cu. For ^{65}Cu there are ^{65}Cu(p, 3n)^{63}Zn reactions that peak for proton energies of 35 MeV and ^{65}Cu(p, X)^{62}Cu that peaks for proton energies of 50 MeV. Very few protons with such high energies were expected, therefore the contribution to the activation expected from reactions with ^{65}Cu will be negligible. It is also possible for γs to activate the copper to ^{62}Cu and ^{64}Cu. Although the cross-sections for the ^{63}Cu(γ, n)^{62}Cu and ^{65}Cu(γ, n)^{64}Cu interactions are smaller than for the protons, a large number of γs may be expected. Therefore, to a good approximation the ^{63}Zn component of the activation is generated only by the proton reactions and can be used to determine the proton spectrum.

The stack composition used for this experiment is given in Table 2. In between the copper foils there were radiochromic film (RCF) layers and CR39 layers. Radiochromic film is sensitive to all ionizing radiations, and changes from clear to blue with an optical density proportional to the dose deposited in the film. CR39 is only sensitive to protons and ions with every stopped particle causing damage that produces a pit once etched in a warm NaOH solution (neutrons can also cause a recorded signal, but the sensitivity is very low).

The activity (counts per second, dN/dt) of each stack layer was determined at three times after the shot. After a decay occurs, the emitted β^+ will be annihilated within

Cu Layer number	Material Material	Thickness (μm)	Cu layer number	Material Material	Thickness (μm)
	Al	25	7	Cu	270
1	Cu	25		RCF (MD-55)	250
2	Cu	50	8	Cu	500
3	Cu	50	9	Cu	500
	RCF (HD-810)	100		CR39	750
4	Cu	100	10	Cu	1000
5	Cu	100	11	Cu	1000
	RCF (HD-810)	100		CR39	750
6	Cu	270	12	Cu	1000

TABLE 2. The composition of the activation stack used to measure the proton spectra.

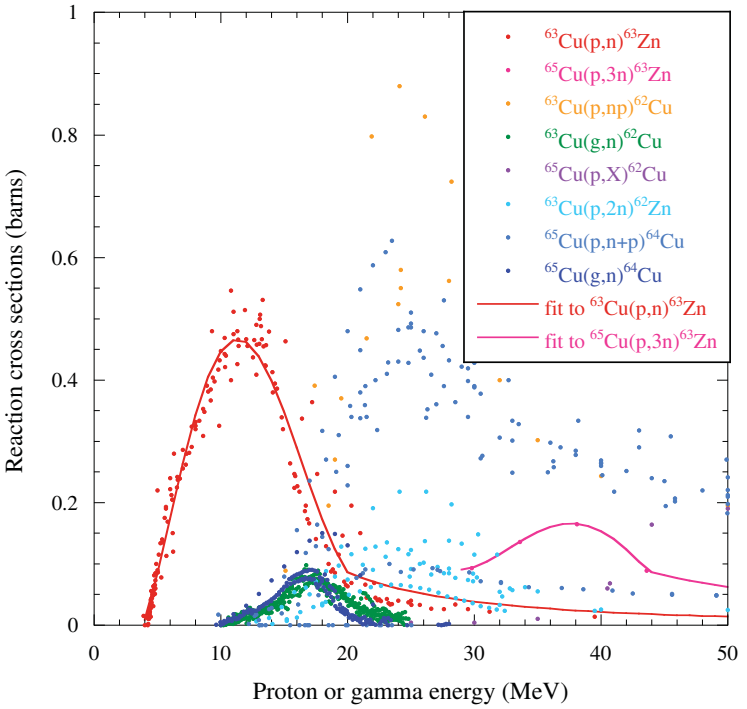

FIGURE 1. Cross-section data for the reactions caused by incident protons and γs likely to generate measurable contributions to the activation. The fits to the reaction with ^{63}Zn products are shown.

the copper, producing two 511-keV photons in opposite directions, distinguishing the β^+ decays from other radiation. The activity for each copper layer was measured by coincidence counting using two scintillator/photomultiplier tubes arranged to measure coincident events from the decaying activated atoms.

The isotopes ^{63}Zn, ^{62}Cu, and ^{64}Cu decay via positron emission with half-lives of $\tau_{\frac{1}{2}} = 38.47$ min, 9.67 min, and 12.70 h respectively. At a time, t, when the sample is measured, the total activity was approximately the sum of the contributions from each of these isotopes:

$$A_{\text{total}}(t) = N_{\text{Zn}}(0)\lambda_{\text{Zn}}e^{-\lambda_{\text{Zn}}t} + N_{\text{Cu62}}(0)\lambda_{\text{Cu62}}e^{-\lambda_{\text{Cu62}}t} + N_{\text{Cu64}}(0)\lambda_{\text{Cu64}}e^{-\lambda_{\text{Cu64}}t}, \qquad (2.1)$$

where $N_{Zn}(0)$, $N_{Cu62}(0)$, and $N_{Cu64}(0)$ are the total numbers of activation at the time of the shot, t_0, and λ_{Zn}, λ_{Cu62}, and λ_{Cu64} are the decay constants given by $\lambda = \ln 2/\tau_{\frac{1}{2}}$ [s^{-1}]. The three measuring times need to be suitably delayed so that the ratio of activities of the different isotopes changes significantly. Then by solving the three simultaneous equations ((2.1) at t_1, t_2, and t_3), the initial numbers of each of the isotopes are found.

Specifically, $N_{Zn,i}(0)$ was determined for each layer, i. The initial proton spectrum, S_j, entering the stack was related to these activations by

$$N_{Zn,i}(0) = \sum_{j=1}^{n} R_{i,j} S_j \triangle E_j, \qquad \text{for } i = 1, 2, \ldots, m, \tag{2.2}$$

where there are n energy bins. $R_{i,j}$ are the average sensitivities (number of activated atoms per incident proton) in the energy bin $\triangle E_j$ for the reactions generating ^{63}Zn.

The energy loss of the protons as they pass through the stack was calculated by considering the dE_p/dx of the different stack materials using the NIST database, PSTAR. A simple code was used to determine the proton spectrum changes using a step thickness, dx. The activation for each layer was calculated by adding the calculated contributions due to the continuously changing proton spectrum. The cross-sections for the ^{63}Cu(p, n)^{63}Zn and ^{65}Cu(p, 3n)^{63}Zn reactions, shown in Fig. 1, were used to find the total ^{63}Zn activation per incident proton in each piece of copper. The sensitivity for a particular layer with a density, ρ, and a thickness, L, to a particular reaction with a cross-section, σ, is therefore given by

$$R_{i,j} = \rho \sigma L, \tag{2.3}$$

and is shown in Fig. 2. The proton spectra was then found using an iterative random perturbation method (Clark 2001).

3. Experimental results

Figure 3(a) shows the number of ^{63}Zn, $N_{Zn}(0)$, produced in the activation stacks as a function of their depth into the stack for the different density targets. These measurements were then deconvolved into the proton spectra shown in Fig. 3(b). The spectra from the 10-μm Mylar target and the 3-mg cm^{-3} foam (the lowest density) were comparable in number and proton energy. The energy conversion efficiencies, from laser energy into proton beam energy (for >4-MeV protons), were 3.1% and 2.6% for the 10-μm Mylar and the 3-mg cm^{-3} foam respectively. The higher density foams have significantly lower proton numbers and maximum energies and the conversion efficiencies were 0.6%, 0.9%, and 1.1% for 20 mg cm^{-3}, 45 mg cm^{-3}, and 100 mg cm^{-3} respectively.

The activated copper pieces were also used as a beam divergence measurement by placing them on image plate detectors to record an activity image (Clarke et al. 2008). Figure 4 compares the beam profiles from the copper activation taken from the second layer of copper (sensitivity peaks at around 12 MeV) with the beam profile on the second layer of RCF (sensitive to protons with energies > 12.5 MeV). The proton beams recorded using both methods are in good agreement, with the RCF providing finer features. The structure of the proton beam at this energy shows some ring-like structure that is not uncommon for this type of experiment (Clark et al. 2000). Also, there are streaked horizontal and vertical features (more pronounced at

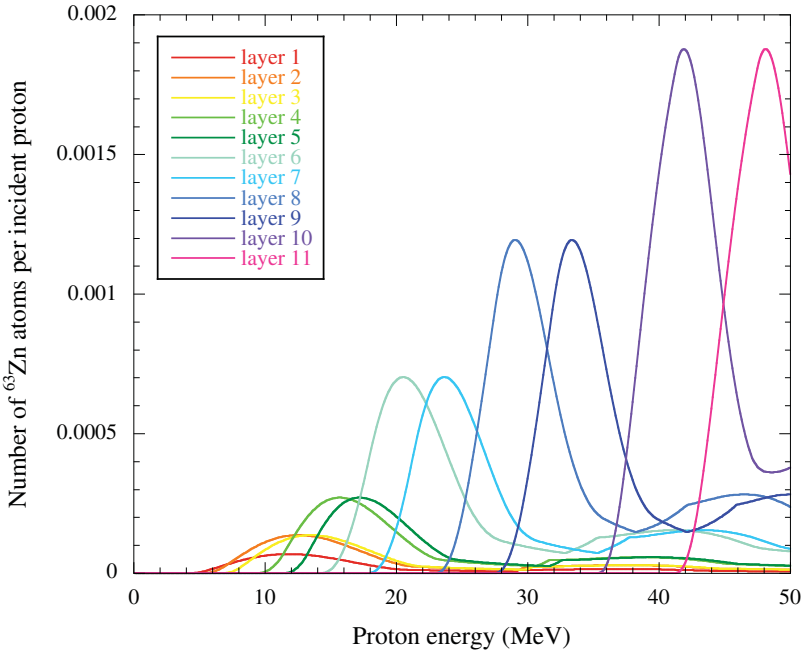

FIGURE 2. The number of ^{63}Zn atoms produced per incident proton entering the activation stack as a function of proton energy for each copper layer.

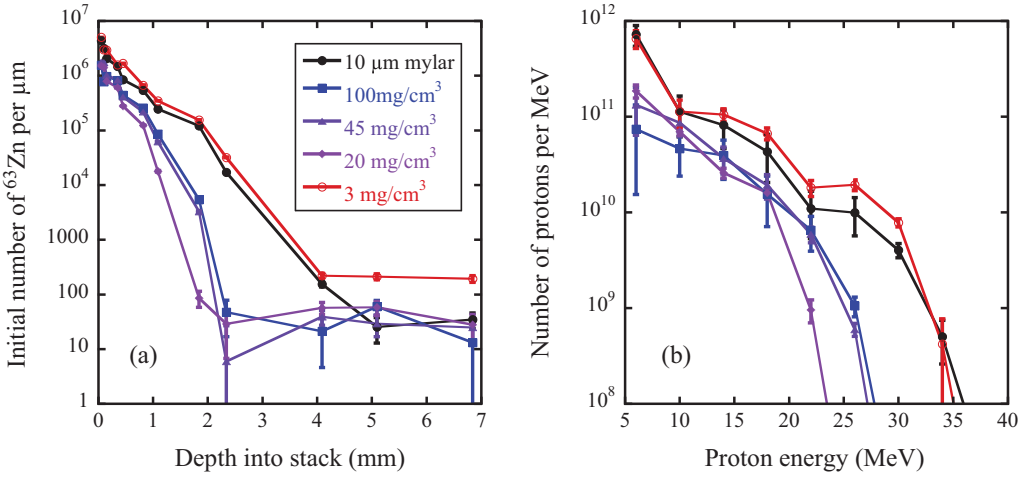

FIGURE 3. (a) The number of ^{63}Zn, $N_{zn}(0)$ generated as a function of depth into the activation stacks for the different density targets. (b) The proton beam spectra deduced from the activation data.

the lower energies) that are likely due to the small spatial size of the square washer (Zepf et al. 2001).

4. Particle-in-cell simulations

A series of relativistic 2D, 3V PIC simulations were performed using the code OSIRIS (Fonseca et al. 2002). A stationary simulation box with a size of 251 μm × 251 μm

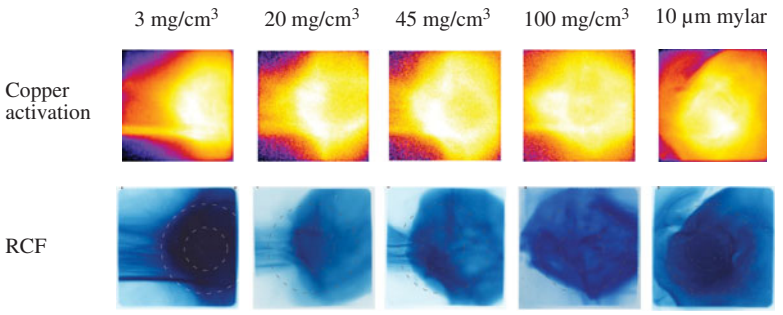

FIGURE 4. Proton beam profiles recorded using the copper activation imaged using image plate detectors and directly on the radiochromic film stack layers for different density targets. The second copper layer image is shown and the radiochromic film image would correspond to proton energies of around 12.5 MeV or greater. The dashed, concentric circles indicate beam half-angle divergences of 10° and 20° centered on the rear target normal axis.

and a resolution of 41.9 cells per λ in the laser-propagation, x-direction and 25.13 cells per λ in the transverse, y-direction was used. The density profile had a 1-μm-long linear density ramp at the front of the plasma, 158 μm of proton plasma at maximum density, a 1-μm linear ramp at the rear of the target into vacuum region. The maximum densities investigated were n_e of $0.9n_c$, $1.5n_c$, $3n_c$, $4.5n_c$, $15n_c$, and $30n_c$. The laser pulse was linearly polarized with the electric field in the y-direction (in the plane of the simulation), with a FWHM $\tau_L = 500$ fs and $\lambda = 1.053$ μm. It was focused to a beam waist $w_0 = 8$ μm at the top of the front density ramp, to give a peak vacuum $a_0 \approx 15$. The lowered value for the simulation a_0 is to account for the electron acceleration via Direct Laser Acceleration (DLA) overestimating the beam energy in 2D simulations due to different scaling of DLA in 2D and 3D.

5. Discussion

The acceleration of the protons from the rear surface via target normal sheath acceleration (TNSA) (Hatchett et al. 2000) is determined by the electric space-charge field set up at the rear target surface interface with the vacuum. The electric sheath field can be enhanced in several ways and can be described by isothermal expansion models (Wilks et al. 2001; Mora 2003) that approximate the peak electric field as $F_0 \approx \sqrt{k_B T_e n_{\mathrm{rear}}/(2\epsilon_0)}$. Therefore an increase in the hot electron temperature, T_e, or density of the hot electrons at the rear target–vacuum interface, n_{rear}, would enhance the electric field and in turn would accelerate higher energy protons. The variation of T_e with target density is non-trivial due to the complexities of the electron acceleration mechanisms. But the variation of n_{rear} with target density is significant and can explain the observed trends.

Figure 5 shows the longitudinal electric fields averaged over a 34-μm region of the center of the box as a function of time into the simulation for each of the target densities. The longitudinal electric field is strongest at the rear target–vacuum boundary ($x = 168$ μm) at around 1.2 ps into the simulation. This is approximately the time that the peak of the laser pulse would take to propagate through vacuum to the boundary. The overall trend was as the target density was reduced, the peak electric field increases and hence higher energy protons are accelerated. This is due to the improved channel formation at lower plasma densities. Also plotted in Fig. 5 as dashed black lines are the position of the end of the channel for each target

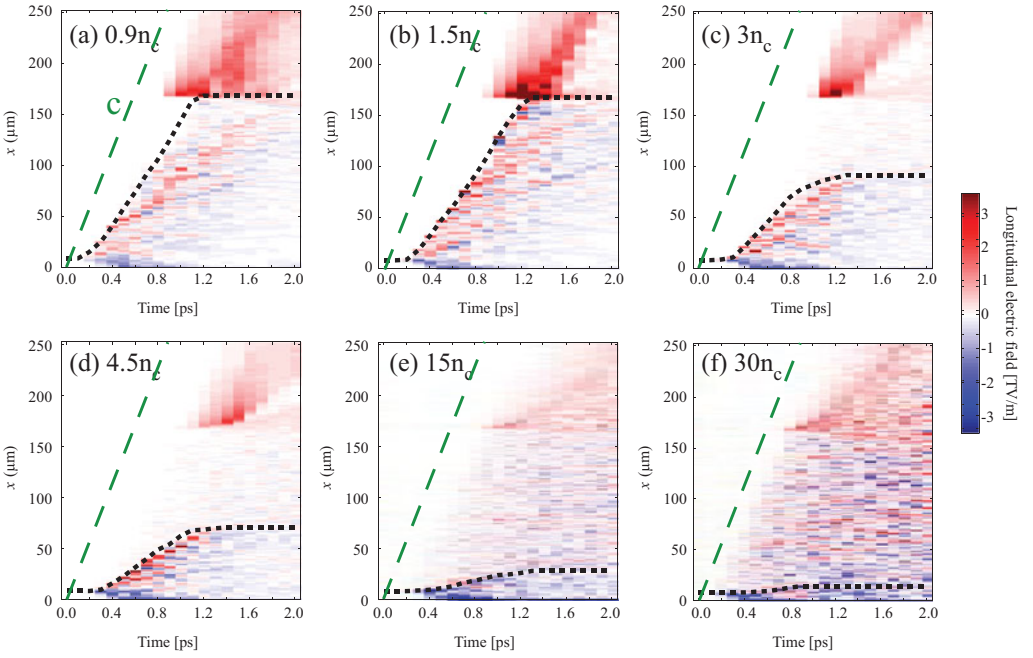

FIGURE 5. The simulation longitudinal electric fields observed as a function of time for the different density simulations. The electric field is averaged in the y-direction over a 34-μm-wide region along the center of the simulation box. The dashed black line shows the position of the end of the channel formed at each time step. The dashed green line shows the speed of light c. The laser pulse peak enters the box approximately 650 fs behind this.

density. The lower the target density, the faster the channel forms and the greater the final channel depth (Willingale et al. 2011). For the lowest densities, $0.9n_c$ and $1.5n_c$, the laser forms a channel all the way through the target. The channel contains radial electric and azimuthal magnetic fields that act to prevent the divergence of the accelerated electron beam. Therefore the longer the channel depth, the stronger the electric field on the rear surface. This trend explains the experimental observations of enhanced proton acceleration from near-critical density targets.

There are a couple of slight inconsistencies between the described trend and the data in Fig. 5. First, the lowest density simulation, $0.9n_c$, had a lower peak electric field than the $1.5n_c$ simulation. This was due to the fact that the electric field was averaged over the central 34 μm of the simulation box to produce Fig. 5. Figure 6 shows the $0.9n_c$ simulation electron density and the longitudinal electric field at 1.2 ps into the simulation. This clearly shows the channel through the $0.9n_c$ plasma was not straight and instabilities such as filamentation (Najmudin et al. 2003; Nilson et al. 2010) and hosing (Naumova et al. 2001) have taken place. Therefore the exit position of the channel, where the hot electron density is the highest, was significantly offset from the center of the box. This means the peak electric field is correspondingly offset from the center of the box and the peak electric field is indeed the largest for the $0.9n_c$ simulation. At the other extreme, the $30n_c$ simulation shows an increase, rather than a decrease in the peak electric field as the channel depth trend would suggest. This is likely due to the increased number of electrons being heated as the target density becomes significantly higher than the relativistic critical density ($n_{\gamma c} = 10.7$ for $a_0 = 15$).

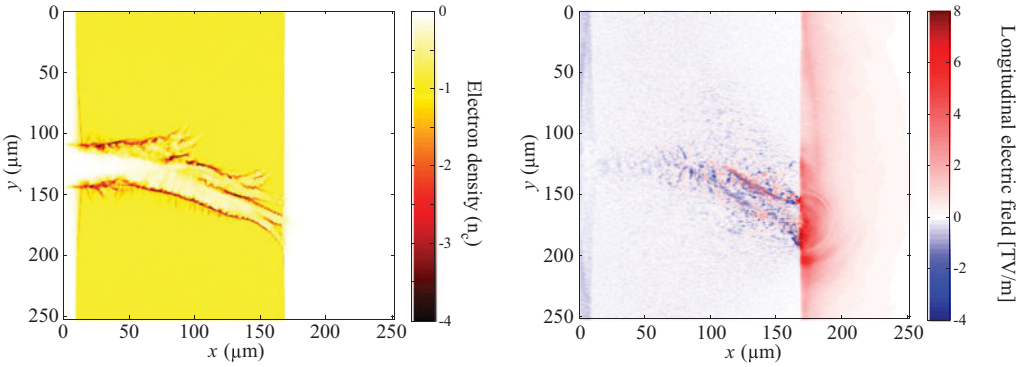

FIGURE 6. The $0.9n_c$ simulation electron density (left) and longitudinal electric field (right) observed at 1.2 ps.

6. Conclusions

In conclusion, the spectra of proton beams accelerated from near-critical density targets were measured using copper activation stacks. The presented experimental measurements show enhanced proton acceleration for near-critical target densities. Particle-in-cell simulations demonstrate that this was likely due to the longer channel formation through lower plasma densities. The radial electric and azimuthal magnetic fields within the channel collimate the hot electron beam, so that the rear surface longitudinal electric field was enhanced and proton acceleration is improved. We have demonstrated that proton beam production can be enhanced in the RIT regime. Careful consideration of target thickness and density can be used to optimise proton beam generation, which could be done using foam targets.

Acknowledgements

The authors gratefully acknowledge the staff of the Central Laser Facility (RAL) for technical assistance and the OSIRIS consortium (UCLA and IST) for the use of the code. The work was funded by EPSRC grant GR/T25934/01.

REFERENCES

Albright, B. J., Yin, L., Bowers, K. J., Hegelich, B. M., Flippo, K. A., Kwan, T. J. T. and Fernández, J. C. 2007 Relativistic Buneman instability in the laser breakout afterburner. *Phys. Plas.* **14**, 094 502.

Clark, E. L. 2001 Measurements of energetic particles from ultra intense laser plasma interactions. *PhD thesis*, University of London.

Clark, E. L. et al. 2000 Energetic heavy-ion and proton generation from ultraintense laser-plasma interactions with solids. *Phys. Rev. Lett.* **85**, 1654.

Clarke, R. J. et al. 2008 Nuclear activation as a high dynamic range diagnostic of laser-plasma interactions. *Nucl. Instrum. Methods Phys. Res.* **585**, 117–120.

Falconer, J. W., Nazarov, W. and Horsfield, C. J. 1995 In-situ production of very-low-density microporous polymeric foams. *J. Vac. Sci. Tech. A* **13**, 1941.

Fiuza, F. et al. 2012 Laser-driven shock acceleration of monoenergetic ion beams. *Phys. Rev. Lett.* **109**, 215 001.

Fiuza, F., Stockem, A., Boella, E., Fonseca, R. A., Silva, L. O., Haberberger, D., Tochitsky, S., Mori, W. B. and Joshi, C. 2013 Ion acceleration from laser-driven electrostatic shocks. *Phys. Plas.* **20**, 056 304.

Fonseca, R. A. et al. 2002 Osiris: a three-dimensional, fully relativistic particle in cell code for modeling plasma based accelerators. In: *Computational Science-ICCS 2002, PT III,*

Proceedings: Lecture Notes in Computer Science, Vol. 2331 (ed. P. Sloot, C. J. K. Tan, J. J. Dongarra and A. G. Hoekstra) Springer-Verlag Berlin, Germany, pp. 342–351.

Haberberger, D., Tochitsky, S., Fiuza, F., Gong, C., Fonseca, R. A., Silva, L. O., Mori, W. B. and Joshi, C. 2012 Collisionless shocks in laser-produced plasma generate monoenergetic high-energy proton beams. *Nature Phys.* **8**, 95.

Hatchett, S. P. et al. 2000 Electron, photon, and ion beams from the relativistic interaction of petawatt laser pulses with solid targets. *Phys. Plasma* **7**, 2076.

Henig, A. et al. 2009 Enhanced laser-driven ion acceleration in the relativistic transparency regime. *Phys. Rev. Lett.* **103**, 045 002.

Mora, P. 2003 Plasma expansion into a vacuum. *Phys. Rev. Lett.* **90**, 185 002.

Najmudin, Z., Krushelnick, K., Tatarakis, M., Clark, E. L., Danson, C. N., Malka, V., Neely, D., Santala, M. I. K. and Dangor, A. E. 2003 The effect of high intensity laser propagation instabilities on channel formation in underdense plasmas. *Phys. Plasma* **10**, 438.

Naumova, N. M., Koga, J., Nakajima, K., Tajima, T., Esirkepov, T. Zg, Bulanov, S. V. and Pegoraro, F. 2001 Polarization, hosing and long time evolution of relativistic laser pulses. *Phys. Plasma* **8**, 4149.

Nilson, P. M. et al. 2010 Plasma cavitation in ultraintense laser interactions with underdense helium plasmas. *New J. Phys.* **12**, 045 014.

Palmer, C. A. J. et al. 2011 Monoenergetic proton beams accelerated by a radiation pressure driven shock. *Phys. Rev. Lett.* **106**, 014 801.

Pukhov, A. and Meyer ter Vehn, J. 1998 Relativistic laser-plasma interaction by multi-dimensional particle-in-cell simulations. *Phys. Plasma* **5**, 1880.

Ridgers, C. P., Brady, C. S., Duclous, R., Kirk, J. G., Bennett, K., Arber, T. D. and Bell, A. R. 2013 Dense electron-positron plasmas and bursts of gamma-rays from laser-generated quantum electrodynamic plasmas. *Phys. Plasma* **20**, 056 701.

Ridgers, C. P., Brady, C. S., Duclous, R., Kirk, J. G., Bennett, K., Arber, T. D., Robinson, A. P. L. and Bell, A. R. 2012 Dense electron-positron plasmas and ultraintense γ rays from laser-irradiated solids. *Phys. Rev. Lett.* **108**, 165 006.

Silva, L. O., Marti, M., Davies, J. R., Fonseca, R. A., Ren, C., Tsung, F. S. and Mori, W. B. 2004 Proton shock acceleration in laser-plasma interactions. *Phys. Rev. Lett.* **92**, 015 002.

Wei, M. S. et al. 2006 Reduction of proton acceleration in high-intensity laser interaction with solid two-layer targets. *Phys. Plas.* **13**, 123 101.

Wilks, S. C., Kruer, W. L., Tabak, M. and Langdon, A. B. 1992 Absorption of ultra-intense laser pulses. *Phys. Rev. Lett.* **69**, 1383.

Wilks, S. C. et al. 2001 Energetic proton generation in ultra-intense lasersolid interactions. *Phys. Plasma* **8**, 542.

Willingale, L. et al. 2009 Characterization of high-intensity laser propagation in the relativistic transparent regime through measurements of energetic proton beams. *Phys. Rev. Lett.* **102**, 125 002.

Willingale, L., Nilson, P. M., Thomas, A. G. R., Bulanov, S. S., Maksimchuk, A., Nazarov, W., Sangster, T. C., Stoeckl, C. and Krushelnick, K. 2011 High-power, kilojoule laser interactions with near-critical density plasma. *Phys. Plasma* **18**, 056 706.

Zepf, M. et al. 2001 Fast particle generation and energy transport in laser-solid interactions. *Phys. Plasma* **8**, 2323.

Culham Prize Winner 2008

Dr Louise Willingale is an Assistant Professor in the department of Electrical Engineering and Computer Science at the University of Michigan. She received her PhD in Plasma Physics from Imperial College London in 2007. Her thesis "Ion acceleration from high intensity laser plasma interactions: Measurements and applications" won the 2008 Culham Thesis Prize for "for significant experimental and numerical work on the acceleration of ions to high energies by laser-plasma interaction", the 2008 European Physical Society Plasma Physics Division PhD Research Award and the 2009 John Dawson Thesis Prize. In 2008 she joined the University of Michigan initially as a postdoctoral fellow and then became an Assistant Research Scientist. Louise primarily studies experimental high-intensity laser-plasma interactions and has performed experiments at facilities such as the Vulcan Petawatt laser (RAL), the Omega EP laser (LLE) and the Titan laser (LLNL) to investigate topics including laser-driven ion acceleration, laser channeling and relativistically induced transparency, magnetic reconnection and magnetic field advection.